

Setting the H-mode pedestal structure: variations of particle source location using gas puff and pellet fueling

A.O. Nelson^{1,3,a}, F.M. Laggner¹, R. Groebner², B.A. Grierson¹,
O. Izacard³, D. Eldon², M.W. Shafer⁴, A. Leonard², D. Shiraki⁴,
A.C. Sontag⁴, E. Kolemen^{3,a} and the DIII-D Team²

¹ Princeton Plasma Physics Laboratory, Princeton, NJ 08543, United States of America

² General Atomics, San Diego, CA 92121, United States of America

³ Princeton University, Princeton, NJ 08544, United States of America

⁴ Oak Ridge National Laboratory, Oak Ridge, TN 37831, United States of America

E-mail: anelson@pppl.gov and ekolemen@pppl.gov

Received 26 September 2019, revised 16 November 2019

Accepted for publication 2 December 2019

Published 21 February 2020



Abstract

Experiments in DIII-D show that a particle source location inside the top of the H-mode pedestal (pellets) maintains a higher pedestal pressure than an edge source (gas fueling) through a widening of the electron temperature pedestal with reduction of the temperature gradient. The effect of these two fueling schemes on the H-mode pedestal structure was examined in DIII-D by comparing controlled pellet-fueled and gas-fueled discharges across a fueling scan up to 40 torr $l\ s^{-1}$. High resolution electron profiles reveal that gas fueling lowers the pedestal pressure as the density profile shifts radially outwards and the separatrix density increases, while pellet fueling maintains a constant pedestal pressure. The neutral source locations from pellets and gas are determined with the PELLET and UEDGE codes, respectively, and quantify the particle source localization. Pellets provide significant ionization inside the pedestal top while gas puffing localizes ionization in the scrape-off-layer and pedestal foot, broadly consistent with the density profile structure influenced by the source. ELMs are observed to increase in frequency and reduce impurity content as fueling is increased. Stability analysis with ELITE shows that both conditions are near the type-I ELM corner of the peeling–ballooning stability diagram, which is altered significantly by the introduction of pellets. Since transport mechanisms are not observed to change substantially with particle source location, wider pedestals allow the pellet-fueled discharges to retain higher pedestal temperatures at similar pedestal densities. EPED1 is tested to capture the pedestal pressure, under-predicting the height with pellets and over-predicting the height with gas by $\sim 15\%$. These results have important implications for future reactors where pellet fueling will be the primary particle source due to an opaque scrape-off-layer by showing that the neutral source location plays a role in setting the structure of the H-mode pedestal.

Keywords: plasma, tokamak, pellet, gas puff, pedestal

(Some figures may appear in colour only in the online journal)

^a Author to whom any correspondence should be addressed.

1. Introduction

For next step devices like ITER, a quantitative understanding of the pedestal as a function of boundary plasma conditions and externally controllable parameters is essential for achieving good performance. Located at the edge of the confined plasma region, the pedestal's structure has a strong impact on core plasma performance and global plasma stability, and is important for mitigating heat flux loads to plasma facing components through events such as edge-localized modes (ELMs) [1–3]. Though many factors such as plasma shaping can influence the structure of the pedestal, several studies have shown that neutral penetration plays an important role [4–6]. Since the neutral source profile for future magnetic fusion devices is expected to change dramatically from fueling profiles currently present in modern tokamaks, the quantitative effect of particle source location on pedestal structure remains an important consideration [7].

Today's experiments typically control the plasma density via gas puffing, which deposits particles outside of the confined plasma. However, as the scrape-off-layer (SOL) becomes hotter and thicker, the ability for neutrals to reach and travel across the separatrix to the confined plasma region decreases and the ionization profile shifts radially outwards. As a result, the pedestal structure is modified as the fueling efficiency of increased gas puffing is reduced [8–10]. At higher fueling levels, experiments on several machines have shown that aggressive gas puffing can lead to degraded H-mode pedestal performance [6, 11–14], though strong deuterium (D_2) gas puffing has also been shown to improve confinement in high powered discharges on DIII-D [15]. In order to continue to fuel the plasma to high densities in next-step fusion devices like ITER, fueling schemes must be able to bypass the SOL and reach the main plasma. For this reason pellet injection, which can transport neutral fuel beyond the SOL and into the main plasma, is projected as the most promising potential candidate for plasma fueling in reactors [4, 16–18]. Pellet injection, however, is also known to perturb the edge stability and thereby the pedestal structure. For example, small pellets have been routinely used to trigger ELMs on many machines [19–23]. In order to maintain edge control during fuel pellet injection, gas and pellet fueling will likely be used in tandem on future machines, complicating the physics setting the pedestal structure [24].

In this context, a pressing question in developing a better quantitative understanding of the pedestal is this: how will changing the neutral fueling profile from an edge-localized scheme (gas puffing) to a more centrally-localized scheme (pellet injection) alter the structure of the H-mode pedestal? Several studies have shown that changing the fueling scheme from gas- to pellet-fueling can have significant effects on the behaviour of the plasma. For example, early experiments on Alcator-C reported higher achievable densities and energy confinement in pellet-fueled experiments compared to similar gas-fueled discharges [25]. This was corroborated on JT-60U, where HFS pellet injection was used to extend the density range of an ELMing H-mode regime, achieving higher pedestal pressures compared to gas fuelled discharges [26]. The

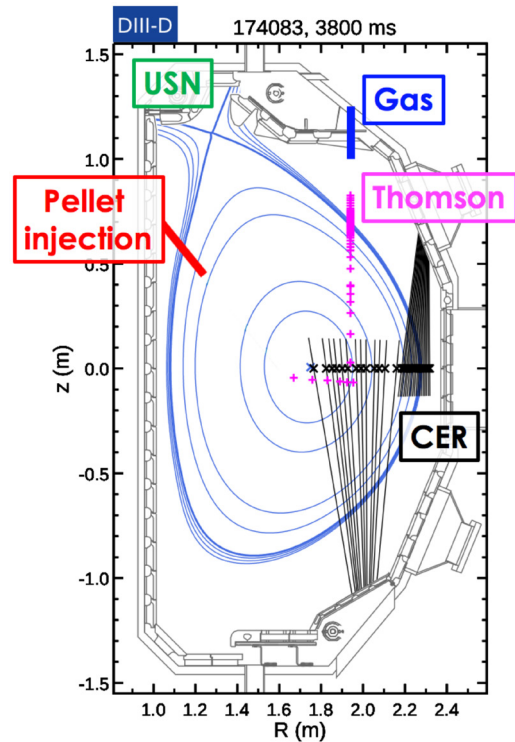


Figure 1. Plasma cross section of a typical discharge used in this study. Pellets are injected from the HFS (red) while gas puffing is applied from the a valve sitting at the LFS top of the machine (blue). The discharges were run in USN to take advantage of the more closed, pumped divertor configuration.

increased pedestal pressure was found to be a result of higher temperatures sustained by both the pedestal width and the pedestal gradient. Similarly, experiments on DIII-D pellet injection from the HFS was shown to be more efficient at fueling the plasma than gas puffing [27]. Pellet fueling has also been shown to lead to different plasma behavior: changing from gas puffing to pellet injection on ASDEX Upgrade was shown to decouple the collisionality at the separatrix and the pedestal top and thereby trigger a resurgence in large ELMs [28]. Changes in the ELM characteristics were invariant on the size or velocity of the injected pellets, suggesting that the fueling mechanism alone plays a key role in defining the pedestal stability. Work to this extent has also been conducted on MAST, where additional microinstabilities were found to be instrumental in relaxing the asymmetric density and temperature profiles caused by pellet injection towards quasi-steady-state (stationary) values [29].

In this paper, we highlight and explain a quantitative characterization of significant changes to the stationary pedestal structure and plasma stability resulting from experimentally controlled changes to the ionization profile. The series of DIII-D discharges described in section 2 were used to determine the effect of the particle source location on the pedestal structure. Though pellets are shown to have a large transient effect on the pedestal top, the main results of this paper (presented in section 3) concern changes to the stationary pedestal structure that result from variations in the particle source location. Notably, pellet injection was shown to increase the pedestal top electron density ($n_{e,ped}$) and flatten the electron

Table 1. Key parameters of the pellet-fueled discharges (bold) and the gas-fueled discharges (italic) are compared. Each fueling scan has a reference plasma with no pellet or gas fueling. Total fueling is the sum of NBI and pellet injection/gas puffs for each shot.

Shot number	Fueling type	Pellet/gas rate (torr l s ⁻¹)	Total fueling rate (torr l s ⁻¹)	P_{ECH} (MW)	P_{NBI} (MW)	β_{N}
174082	NBI only	0	10.5	0	4.67	2.0
174084	NBI + pellets	11.1 (3 Hz)	21.6	0	4.67	2.0
174086	NBI + pellets	18.5 (5 Hz)	29.0	0	4.64	2.0
174083	NBI + pellets	25.9 (7 Hz)	36.4	0	4.66	2.0
174092	NBI + pellets	37.0 (10 Hz)	47.5	0	4.63	2.0
<i>174080</i>	ECH + NBI	0	3.3	3.09	1.56	1.5
<i>174088</i>	ECH + NBI + <i>gas</i>	12.1	15.3	3.08	1.54	1.3
<i>174089</i>	ECH + NBI + <i>gas</i>	21.1	24.5	3.09	1.57	1.4
<i>174091</i>	ECH + NBI + <i>gas</i>	27.2	30.5	3.08	1.57	1.3
<i>174090</i>	ECH + NBI + <i>gas</i>	33.2	36.5	3.10	1.56	1.3
<i>174095</i>	ECH + NBI + <i>gas</i>	42.3	45.6	3.09	1.55	1.3

temperature gradient in the pedestal. Gas fueling was shown to shift the density profile radially outwards relative to the temperature profile and to increase the SOL electron density ($n_{e,\text{sep}}$). In section 4, details concerning ELM characteristics are coupled to a brief analysis of modifications to the peeling–ballooning stability boundary. Finally, in section 5, a suite of modeling tools is used to characterize the fueling profiles and transport coefficients, showing that changes in the particle source location can directly explain observed differences in the pedestal structure. The conclusions are summarized in section 6 and are presented along with suggestions for future work.

2. Experimental methodology

The following describes a set of experiments in which the H-mode pedestal structure was observed to depend on the particle source location. Different particle source locations were achieved by comparing gas- and pellet-fueled discharges, keeping the total fueling rate, the total heating power and the pedestal pressure as similar as possible.

2.1. Experimental setup

Because of the non-metallic vessel wall, high plasma performance can be realized at DIII-D without requiring external gas puffing throughout the shot. This affords an opportunity to directly study the impact of the particle source location on plasma performance by controllably alternating between gas- and pellet-fueled discharges. In this experiment, gas puffing was compared to pellet injection over a series of discharges. The particle source profile was further controlled by running in the upper single null (USN) configuration with reversed B_t direction (favorable ion $B \times \nabla B$ drift towards the upper X-point) shown in figure 1. The plasma shape had elongation $\kappa \sim 1.8$ and triangularity $\delta \sim 0.7$. This configuration was chosen to take advantage of the more-closed upper divertor, which consists of a dome and an outer baffle and allows for more potent pumping of residual neutrals, reducing the

recycling influx of wall materials from the strikepoint back into the plasma [30]. Helium glow discharge cleaning was also performed between plasma shots to reduce the wall inventory. The plasma shape was optimized to achieve good divertor closure and to provide excellent profile diagnostic coverage of the edge to properly resolve the pedestal. Combined, these efforts allow for a simpler comparison between experimentally imposed fueling profiles by minimizing the recycling term in the source profile.

In this chosen geometry, two fueling scans up to ~ 50 torr l s⁻¹ were completed over a series of discharges. After the administration of an identical prefill gas in the beginning of each shot, the particle source location was varied experimentally starting at 2 s by fueling with either gas puffing or pellet injection. Total fueling rates and heating powers for each discharge are listed in table 1. The injected pellets were cylindrical frozen D_2 fueling pellets with length = diameter = 1.8 mm, and had an average speed of ~ 160 m s⁻¹ with minimal ($< 10\%$) residual gas injection. Pellets were injected from the high-field side (see figure 1) to achieve maximum neutral penetration and fueling efficiency due to an inward $\nabla B \times B$ drift [31, 32]. The gas-fueled discharges used main-chamber fueling with D_2 gas puffed from a valve located at the top of the machine on the low-field side, as shown in figure 1. The total fueling rate, defined as the total number of particles entering the DIII-D vacuum vessel as a function of time, was matched across the two fueling scans for direct comparison of the effects of particle source location. Comparisons of shots with similar density was also possible, as shown in figure 2, where time traces for a pellet-fueled and a gas-fueled discharge with different total fueling rates are plotted. All plasma discharges were performed at a plasma current (I_p) of 1 MA, toroidal magnetic field (B_t) of 2 T and a moderate Greenwald fraction of $n_e/n_{\text{GW}} \approx 0.4$, where n_{GW} is the Greenwald density. The edge safety factor across both fueling scans remained unchanged with q_{95} around 5.3. The ELM frequency increased steadily across each fueling scan from relatively large and slow type-I ELMs in the reference cases towards a mixture of small and large ELMs at frequencies upwards of ~ 300 Hz by end of the achieved fueling scan. No significant difference in

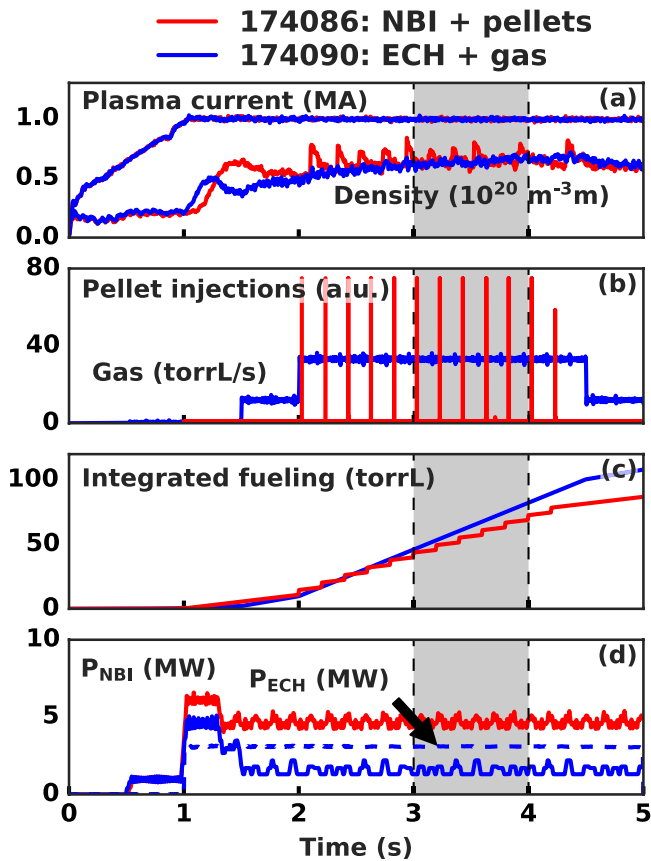


Figure 2. Comparison of key parameters for discharges 174086 (pellet-fueled) and 174090 (gas-fueled), which have similar densities but *different* fueling rates. The shaded region is the time period considered for analysis. Plotted time traces are (a) plasma current and line-averaged density, (b) gas puff rate and pellet injection times, (c) total integrated fueling (including fueling from NBI) and (d) NBI and ECH heating power. Note that the prefill gas responsible for the initial density rise at $t < 1.5$ s the H-mode onset is not shown here. The prefill gas was identical for each shot.

ELM behaviour was observed between gas- and pellet-fueled discharges.

In order to achieve maximum variation in the particle source location, the heating scheme was varied in conjunction with the fueling source. Pellet-fueled discharges in this study were heated with ~ 4.6 MW neutral beam injection (NBI), which also contributed some additional core fueling (~ 10.5 torr $l s^{-1}$) in order to accentuate the more central-localized fueling profile. In contrast, the gas-fueled discharges were dominantly heated by ~ 3 MW electron cyclotron resonance heating (ECH). This limited any central fueling that would occur in the gas-fueled shots, though ~ 1.6 MW NBI power was still required for diagnostic purposes, as noted in table 1. Note that the total heating power between the two fueling scans remained well-matched. Variations in the heating schemes, however, produced changes in the global confinement, with thermal energy confinement with ECH being $\sim 1/2$ the confinement with NBI. These effects were initially underestimated and are covered in more detail below. Due to additional neutral beam injection, the pellet-fueled cases had $\beta_N \approx 1.9$ – 2.0 , which was higher than the gas-fueled

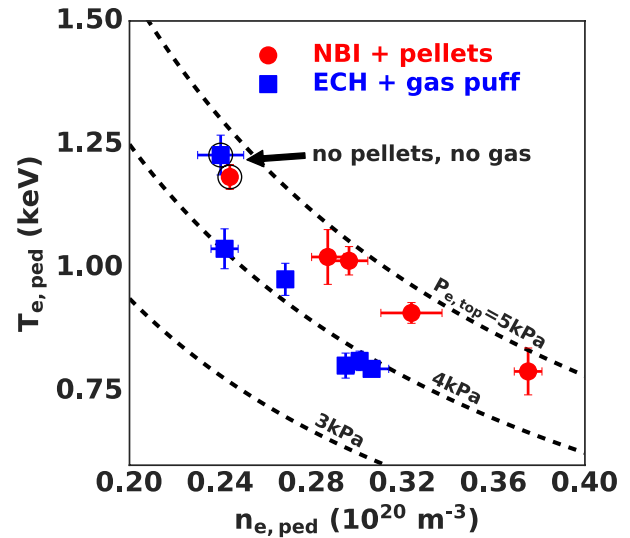


Figure 3. Pedestal top density and temperature for the pellet-fueled scan (red) and the gas-fueled scan (blue). Each fueling scan remains at nearly constant $p_{e,ped}$ across the database. Circled points have no additional pellet or gas fueling beyond the minimal prefill gas administration.

cases, which had $\beta_N \approx 1.3$ – 1.5 (see table 1). The variation in β_N between the two fueling scans can be attributed to the additional NBI heating present in the pellet-fueled cases, which contributes to better confinement by directly heating the ion population. It should also be noted that changes between ECH and NBI resulted in some profile changes in the core region. Specifically, the NBI-heated discharges have additional density peaking inside of $\psi_n \sim 0.25$, which leads to $\sim 10\%$ higher on-axis electron densities. Correspondingly, the ECH-heated discharges have elevated electron temperature peaking inside of $\psi_n \sim 0.4$. These well-established effects are highly core-localized and not expected to heavily influence the pedestal profiles.

Constant pedestal top pressure was generally maintained across each individual fueling rate scan (see figure 3,) showing that the pedestal temperature and density remained strongly coupled regardless of the fueling scheme and indicates conservation of pedestal stored energy. Observed changes in the plasma profiles that result from variations in the neutral fueling source thus result from the coupled structural modifications of the density and temperature pedestals that are the subject of this paper. Variation in the amplitude of a core $n = 2$ tearing mode may contribute to some alteration in the electron pressure during the gas fueling scan, but does not explain the full $p_{e,ped}$ drop observed at the beginning of the gas scan. Note that increases in the gas fueling rate at Greenwald fractions larger than those reached in this study have been shown to decrease pedestal performance (temperature and pressure) in DIII-D [14]. This high-density regime was avoided in order to facilitate comparison with the pellet-fueled cases, which were limited in density by the maximum achievable pellet injection rate.

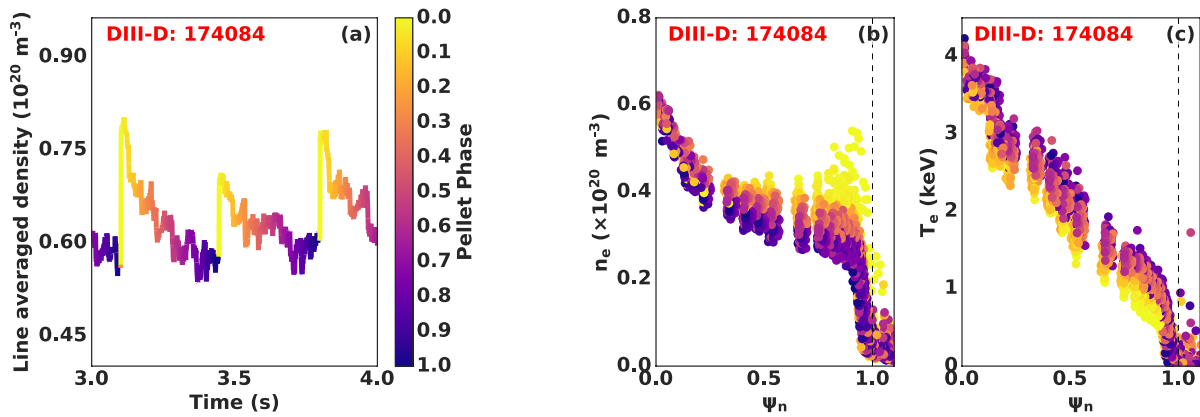


Figure 4. Raw Thomson scattering data colored as a function of time after pellet injection for DIII-D discharge 174084 (3 pellets/second). (a) Line averaged density was binned by phase of the pellet cycle. (b) Electron density peaks sharply at the pedestal top upon pellet injection with core densities as far in as $\psi_n \sim 0.4$ also rising. (c) Electron temperature decreases upon pellet injection.

2.2. Stationary profile analysis

Detailed pedestal analysis of these shots was made possible by the high spatial and temporal resolution of diagnostics on DIII-D. The key measurements for this study were the electron temperature (T_e) and electron density (n_e) profiles provided by a multipulse Thomson scattering (TS) system [33, 34]. Thomson data was obtained every several milliseconds throughout the plasma discharge and has high spatial resolution at the plasma edge to fully measure the pedestal structure. Additional carbon density (n_C) and temperature (T_C) was collected with several charge-exchange recombination (CER) diagnostic systems aimed at the neutral beams [35]. Intrinsic carbon populations are present in DIII-D as a result of chemical and physical erosion from the carbon walls. For the gas-fueled cases, impurity data from CER was scarce due to the low levels of applied NBI. Measurements were mapped to kinetic equilibrium generated with external magnetic data and internal pressure and current constraints [36]. In the kinetic equilibrium, the pressure constraint is the experimental total pressure, which includes electron pressure from TS, impurity ion pressure from CER and modeled main ion and fast ion pressures. The current constraint is taken from motional Stark effect measurements in the core in conjunction with a modelled edge current that includes the Sauter bootstrap current, the NBI-driven current, the Ohmic current and a small poloidal current [37]. Iterations were performed upon the kinetic equilibria to better match the original experimental profiles.

All data were obtained in ELMing H-mode discharges. Periodic ELM crashes correspond to significant modification and depletion of the pedestal. To separate these modulations from underlying structural changes, it is necessary to filter-out modulation of the profile by ELM crashes and pellet injection. See section 4 for a more through discussion of the ELM characteristics. In this work we refer to the filtered inter-ELM profiles as *stationary* profiles. For improved statistics, data was collected over a long time period (1 s) for each discharge, as seen in figure 2. Before fitting, the raw data is filtered as a function of both ELM and pellet cycles: only data in the later part of an ELM cycle (60%–98%) and the later half of a pellet cycle (50%–98%) was included for analysis. The pellet cycle

is defined as the fraction between pellet injection times, during which the density recovers from a pellet-induced spike to the stationary values. This is explained visually in figure 4 where the density spike following pellet ablation can be clearly seen in both Thomson scattering and interferometry data. Upon the injection of a pellet, most of the pellet mass is immediately flushed out of the plasma through ELMs and transport while the remaining raises the density as far in as $\psi_n \sim 0.4$. On the order of $\sim \tau_p$, the pedestal then recovers to a quasi-stationary condition. This transient nature of the pellet-fueled profiles could be considered the biggest difference between the gas- and pellet-fueled cases. To better compare the underlying profile structure with the gas cases, only data from the time period corresponding to quasi-stationary conditions at the end of the pellet cycle was considered. The stationary experimental profiles (n_e , T_e , p_e , n_C and T_C) were fit by modified hyperbolic tangent (mtanh) curves as functions of normalized poloidal magnetic flux ψ_n in order to parameterize their values in the edge region [38]. Due to uncertainties in equilibrium mapping and the spatial location of experimental data, the profiles were shifted to align with a constant value of $T_e = 80$ eV at the separatrix, which is a typical value for DIII-D plasmas and agrees with the two-point model [39]. All profile analysis was completed within the OMFIT [40] framework. Profile fitting was done with OMFITprofiles [41], and kinetic equilibrium reconstructions were produced with CAKE [36].

3. Changes in stationary pedestal structure

The two fueling scans studied here support the claim that the particle source location plays an important role in setting the structure of the H-mode pedestal. Broadly speaking, changes in the pedestal structure were found to be more dramatic in response to changes in the neutral fueling near the pedestal location with gas and pellets than to additional core fueling from NBI. Pellet injection is shown to be more efficient than gas puffing, leading to larger rises in $n_{e,ped}$ at similar fueling rates with no evidence of hitting the Greenwald density limit over the achieved fueling range. The link between the separatrix density $n_{e,sep}$ and the pedestal top density $n_{e,ped}$ is stronger

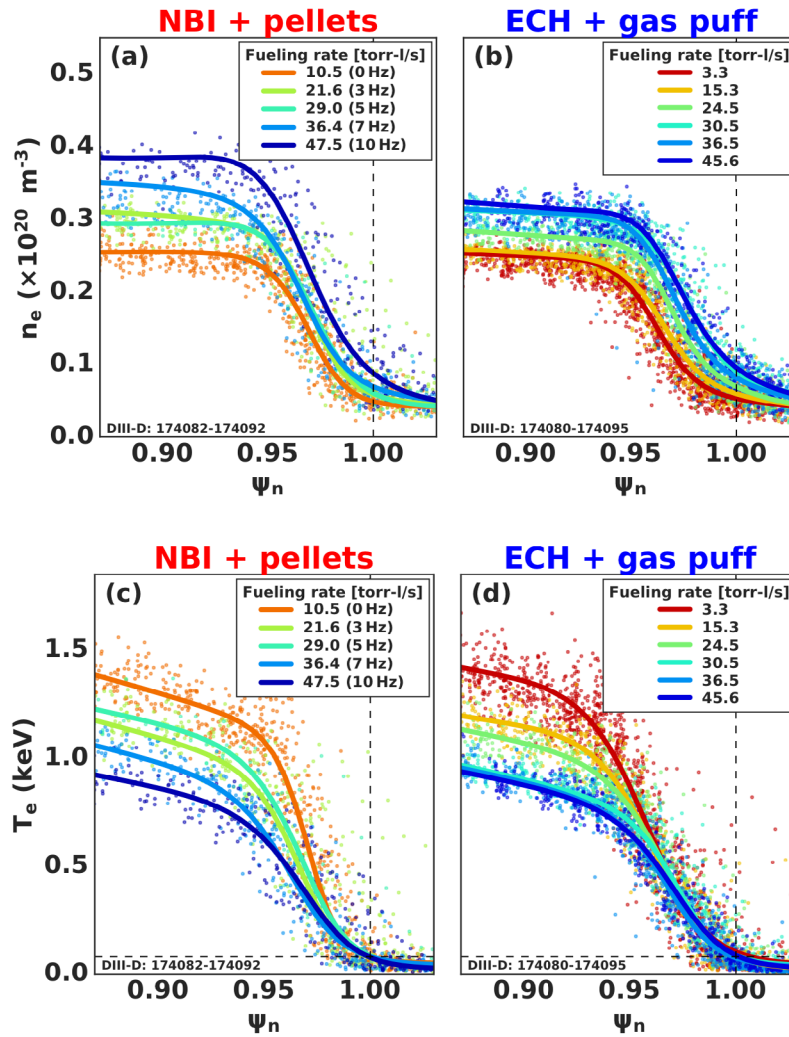


Figure 5. (a) and (b) Electron density and (c) and (d) temperature profiles in the pedestal region for the fueling each fueling scan. Same-color profiles have similar total fueling rates (e.g. 174083: 7 Hz pellet-injection \approx 174090: 33 torr l s^{-1} gas-puffing.)

in the gas-fueled discharges, where the density pedestal is observed to shift radially outwards with respect to the temperature pedestal as the fueling rate is increased. In general the pedestal temperature is found to degrade with increased fueling. Pellet injection is shown to significantly flatten the temperature gradient ∇T_e in the pedestal, whereas gas puffing contributes to a lower $T_{e,\text{ped}}$ without significantly affecting the temperature gradient. This sustains a wider and steeper pressure pedestal in the pellet-fueled discharges, which contributes to better plasma performance (higher $p_{e,\text{ped}}$ at similar density.) These observations are quantitatively categorized below.

3.1. Pedestal density

Fits to the electron density and temperature profiles of the two fueling scans are presented in figure 5. The two reference discharges (no-gas and no-pellets; red traces) are fueled only with NBI and show very similar pedestal structures, despite different NBI fueling levels. Larger changes in the density pedestal structure are observed throughout the gas- and

pellet-fueling scans. In the gas-fueled fueling scan, the pedestal top density $n_{e,\text{ped}}$ increased 130% from 2.4×10^{19} to $3.1 \times 10^{19} \text{ m}^{-3}$ over a total increase in fueling of $42.3 \text{ torr l s}^{-1}$. In comparison, the pellet-fueled cases showed a greater (150%) increase in $n_{e,\text{ped}}$ over a smaller increase in fueling: 2.4×10^{19} to $3.7 \times 10^{19} \text{ m}^{-3}$ over an increase in fueling of 37 torr l s^{-1} . This immediately suggests that pellet-fueling is more efficient than equivalent gas-puffing. Furthermore, the three gas-fueled cases with the highest fueling rates demonstrate only marginal ($<2\%$) increases in $n_{e,\text{ped}}$, whereas n_e has no apparent saturation level in the pellet injection fueling scan ($n_{e,\text{ped}}$ continues to increase even at the highest achievable fueling rates.) Note that in both cases, the separatrix density $n_{e,\text{sep}}$ increased by $\sim 30\%$ across the fueling scan.

Both the width of the density pedestal (defined as the full width from the mtanh fit) and the maximum density gradient $\nabla n_{e,\text{max}}$ remained roughly constant throughout the scan, as shown in figure 6. The density gradient at the separatrix $\nabla n_{e,\text{sep}}$, however, increased by a factor of ~ 3 . It is also apparent that, for the gas-fueled cases in particular, the

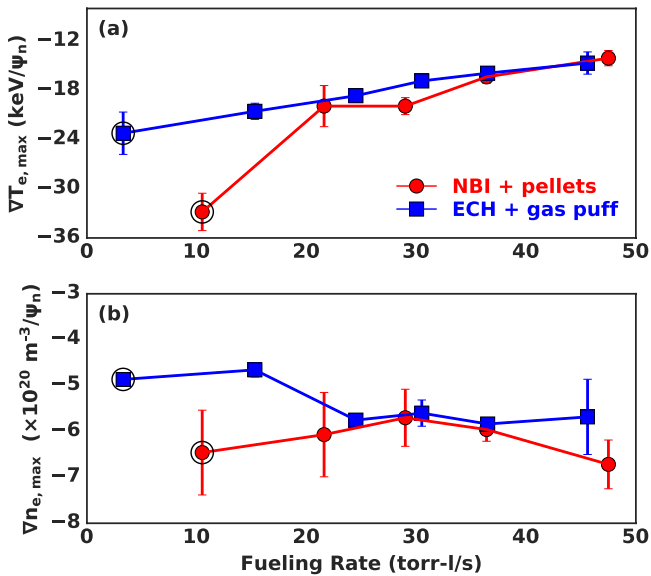


Figure 6. Gradients in the pedestal region. (a) The T_e profile gets flatter with increased fueling while (b) the n_e profile gradient stays approximately constant. Circled points have no pellet or gas fueling.

density pedestal shifts outwards with respect to the temperature profile as the fueling rate increases. In the gas-fueled scan, the steepest gradient region in the n_e profile consistently shifts radially outwards from $\psi_n = 0.96$ to $\psi_n = 0.98$ over the obtained fueling rates. Only at the highest achieved density does the pellet-fueled density display a similar shift. The ratio between the density pedestal top and the separatrix density ($n_{e,\text{ped}}/n_{e,\text{sep}}$) remains roughly constant at $n_{e,\text{ped}}/n_{e,\text{sep}} \sim 3.7$ throughout the gas fueling scan, but increases from 3.8 to 5.1 across the pellet fueling scan, indicating a larger effect on the pedestal structure for the pellet-fueled cases due to the central fueling of $n_{e,\text{ped}}$. The core plasma density increased proportionally with the pedestal density height in both fueling scans.

Observations of effects on the density profile indicate that pellet injection, which deposits the neutrals further inside the confined plasma region, is more efficient at fueling the plasma than gas puffing [42]. To confirm this, the fueling efficiency (defined as the increase in the number of plasma electrons compared to the reference discharge divided by the number of injected gas/pellet particles per second) was calculated for each shot. The average fueling efficiency for the pellet-fueled shots $11 \pm 2\%$, which is $\sim 2\text{--}3$ times higher than the efficiency of the gas-fueled shots, which was $4 \pm 2\%$. The increase in fueling efficiency in the pellet-fueled cases is in part due to direct *neutral fueling* of the core plasma as opposed to predominantly *ion fueling* in the gas cases, where neutral fuel is ionized in the SOL and relies on transport to cross the separatrix. In both fueling schemes, the shot with the lowest fueling rate fell outside the standard deviation. The fueling efficiency for the lowest-dose ($12.1 \text{ torr l s}^{-1}$) gas puff case is $\sim 0\%$ since the first gas exposure serves only to cool the plasma and does not contribute significantly to plasma fueling, as seen in figure 5. In the pellet-fueled cases, however, the lowest pellet-injection rate ($3 \text{ Hz} / 11.1 \text{ torr l s}^{-1}$) has the highest fueling efficiency of all shots at nearly $\sim 15\%$. The high efficiency of

the first pellets is a result of a structural shift in the pedestal that is discussed later in more depth.

Differences in the fueling efficiency of gas puffs and pellets are also evident at higher fueling rates, where opposing trends emerge. After stabilizing around 5%, the efficiency of gas-fueled starts to decrease (dropping by $\sim 20\%$ of its total value from over the last three shots,) suggesting that, in contrast to additional pellets, the majority of the additional gas does not reach the main plasma due to a self-screening effect where the gradient scale length of the density profile remains essentially fixed, leading to linearly scaled n_e profiles. This observation is consistent with investigations on Alcator C-Mod at similar Greenwald fraction, where the pedestal height was reported to increase with the square root of the overall neutral flux [10, 11]. In comparison, the efficiency of the highest-fueled pellet-fueled cases is nearly constant since ablation of the pellets is less dependent on increases in the SOL density.

3.2. Pedestal temperature

As the electron density increases, the electron temperature T_e must decrease if the pedestal pressure p_e is limited to a constant maximum value. For both fueling schemes, this decrease in T_e was accompanied by a decrease in the maximum temperature gradient in the pedestal $\nabla T_{e,\max}$, as shown in figure 6. However, $\nabla T_{e,\max}$ experiences a larger drop by a factor of ~ 2 in the pellet-fueled cases compared to the gas-fueled cases for comparable rises in the fueling rate. Most noticeably, the biggest change in $\nabla T_{e,\max}$ is between the 0 Hz (100% NBI fueled) and the 3 Hz pellet-fueled cases, showing that the initial addition of pellets to a plasma has a much larger effect on the pedestal temperature gradient ∇T_e than the use of either additional pellets or gas puffs. The temperature gradient at the separatrix $\nabla T_{e,\text{sep}}$ remains constant throughout both fueling scans. The T_e pedestal width in the pellet-fueled undergoes a substantial ($\sim 30\%$) increase between the highest density discharge and the reference ‘no pellet’ case while the temperature pedestal width in the gas-fueled cases remains constant. The core plasma temperature decreased proportionally with the pedestal temperature in both fueling scans.

The exaggerated decrease in $\nabla T_{e,\max}$ and corresponding increase in the temperature pedestal width that is observed across the pellet-fueled scan has a simple physical explanation. In the pellet-fueled cases, cold neutrals are deposited further within the plasma compared to the more edge-localized gas administration. As the plasma cools, the pellets are able to travel further towards the core before ablation. Greater quantities of cold fuel deposited further inside the separatrix bring down T_e farther away from the edge, decreasing the temperature gradient ∇T_e in the pedestal. The decreasing ∇T_e in the pellet-fueled cases necessitates an increase in the T_e pedestal width in order to recover the natural plasma pressure. This is discussed in terms of peeling–ballooning stability in section 4.1. Flattening of the temperature profile upon the injection of fueling pellets was also reported in [29].

As shown in figure 3, the absolute magnitude of the temperature pedestal remains well-coupled to the density

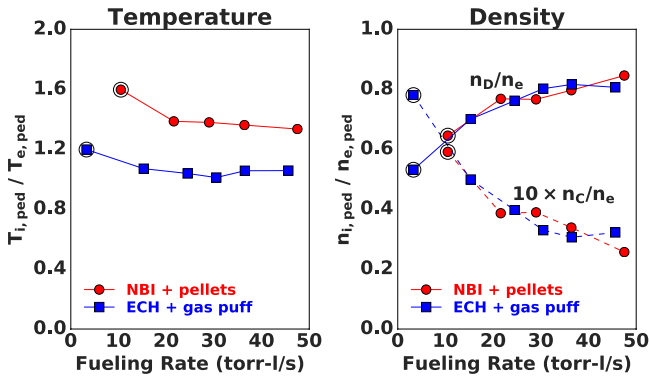


Figure 7. Left: $T_i = T_C = T_D$ decreases proportionally with decreasing T_e for increased fueling. Pellet-fueled cases have hotter ions due to higher NBI heating. Right: with increased fueling, the main ion fraction increases and was accompanied by a decrease in the carbon impurity fraction. Circled points have only beam fueling.

pedestal height such that $p_{e,ped}$ is approximately constant over the obtained fueling rates. Throughout the pellet-fueling scan, $p_{e,ped}$ remained constant at level of the ‘no pellet’ reference case (4.7 ± 0.1 kPa.) However, during the gas-fueling scan, $p_{e,ped}$ dropped by more than 10% from 4.6 kPa in the ‘no gas’ reference case to 4.0 kPa upon the first application of additional gas puffing ($12 \text{ torr } 1 \text{ s}^{-1}$). Further gas-fueling did not change the measured pressure. Note that while variations in the amplitude of a core $n = 2$ mode are observed in the gas scan, the mode is absent in discharges 174080 and 174089, implying that the temperature and pressure drop relative to baseline in the gas-fueled cases regardless of the mode strength. The differences in $p_{e,ped}$ between the gas- and pellet-fueled discharges can then be largely explained by modifications to the structure of the temperature profiles. In the gas-puffing cases, the primary effect of additional gas puffing on top of the ‘no gas’ reference case is to reduce $T_{e,ped}$. Since the plasma is only cooled by the $12 \text{ torr } 1 \text{ s}^{-1}$ gas administration ($n_{e,ped}$ remains constant,) the pedestal pressure drops. For higher doses of gas puffs the temperature is low enough for neutrals to penetrate the confined plasma region, allowing $n_{e,ped}$ to rise and maintain constant $p_{e,ped}$. This is in contrast to the pellet-fueled cases, where the primary effect of the first pellets is to widen the temperature pedestal by flattening ∇T_e . Since neutrals are deposited within the confined plasma region even at the slowest (3 Hz) pellet injection frequency, $n_{e,ped}$ and $T_{e,ped}$ remain well coupled throughout the entire fueling scan.

3.3. Changes in the ion profiles

The effect of increased fueling on the ion profiles was also investigated. Ion data was extracted from intrinsic carbon measurements gathered with charge exchange recombination spectroscopy (CER). Both the impurity ion temperature (T_C) and the impurity ion density (n_C) were shown to decrease with increased fueling. As shown in figure 7, the temperature of the ions tracks $T_{e,ped}$ to within $\sim 20\%$ throughout the fueling scan, though ions are comparatively hotter in the pellet-fueled discharges due to their additional NBI heating. This suggests that the heat fluxes arriving at the pedestal top are also

invariant across the scan, with additional fueling not affecting core power flows. However, n_C does not track with the electron density. The impurity ion ratio (n_C/n_e) decreases as the fueling rate increased in both the gas-fueled and pellet-fueled cases at a rate faster than that predicted by fixed dilution of the impurity species. In correspondence, the main ion ratio (n_D/n_e) was shown to grow with increased fueling across both scans. Here the main ion density is calculated from the charge neutrality constraint between the n_e and n_C measurements. These results show that, regardless of the fueling mechanism, increased fueling is linked to higher purity tokamak plasmas.

The drop in impurity density as a function of increased fueling is correlated with an increased ELM frequency (discussed below.) While large ELMs can source wall impurities and are a serious limiting factor to PFC lifetimes, small ELMs can increase impurity screening in the pedestal and limit the build up of core impurity concentrations [21]. In this study increased fueling rates were correlated with an increased frequency of small ELMs, which likely contribute to the decreasing impurity density. Increased D_2 fueling rates also lead to changes in divertor conditions (eg. temperature or sputtering and erosion rates) that can further affect the main plasma impurity concentration. Such plasma material interactions are beyond the scope of this work.

4. Characterization of ELM behavior

In addition to producing structural changes in the electron pedestal profiles, increases in the fueling rate modify the ELM characteristics by decreasing the average ELM size and increasing the ELM frequency. Since unmitigated type-I ELMs will not be tolerated in ITER, replacing type-I ELMs with smaller, less damaging ELMs is an important topic. In [28], switching from dominant gas-fueling to pellet-fueling is shown to lead to a higher fraction of large type-I ELMs. However, the absence of large ELMs observed in the gas-fueled plasma was also shown to be strongly dependent on the plasma configuration. In this experiment, no significant difference in the ELM behavior is noted in pellet-fueled or gas-fueled discharges, supporting the claim that plasma shaping is critical to the suppression of large type-I ELMs with gas puffing. Further, while pellet-injection is a well-established ELM triggering method, the natural ELM frequency in this experiment was significantly larger ($\sim \times 30$) than the maximum pellet-injection rate, so the ELM-triggering effects of pellets were not distinguishable from the background ELMs. Here, increased fueling is linked to an increase in the ratio of small ELMs to large ELMs, where large ELMs are associated with visible ($>2\%$) drops in the the plasma stored energy W_{MHD} . To this end, W_{MHD} was calculated with the EFIT code [43] as a function of time for each discharge. The total ELM frequency (f_{ELM}) increased for both small and large ELMs as a function of increasing fueling rate, regardless of the fueling scheme.

As reported in figure 8(a), f_{ELM} increases as a function of increased fueling rate in both the pellet-fueled and the gas-fueled cases. For both reference cases, the ELMs

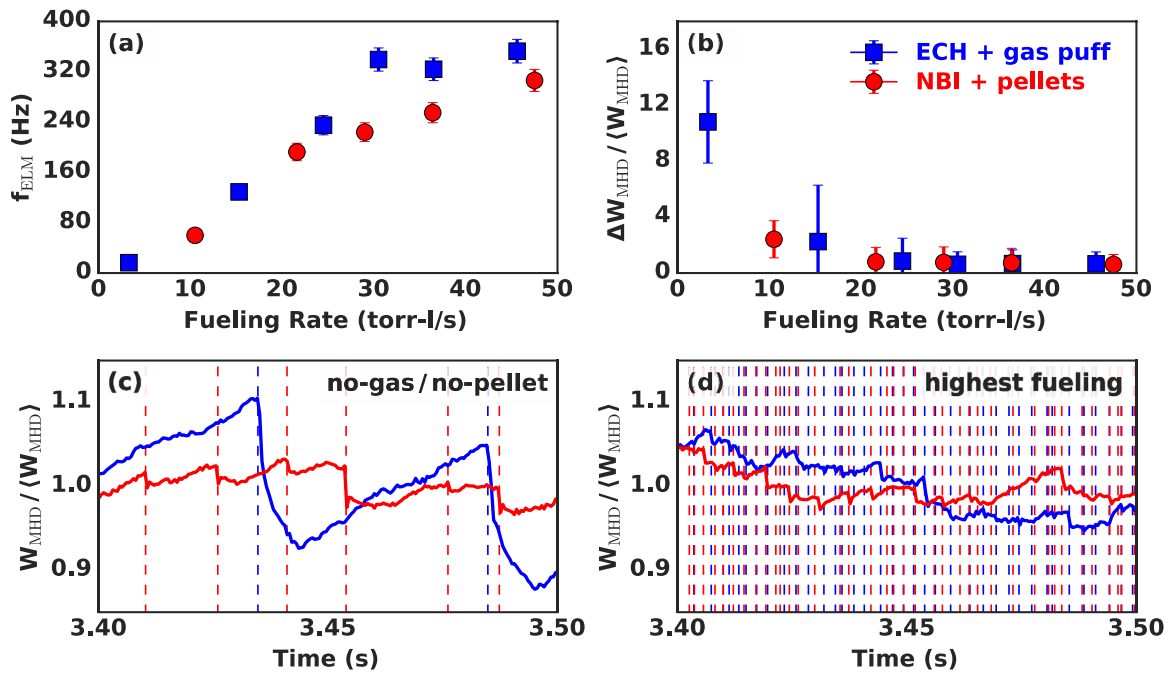


Figure 8. Characterization of observed ELMs. (a) ELM frequency increases with increased fueling rate. (b) The average size of the ELMs, as determined from ΔW_{MHD} drops with increasing frequency. (c) and (d) W_{MHD} as a function of time for select shots. Dashed vertical lines mark the ELM times.

are primarily large, type-I ELMs with relatively slow f_{ELM} : $f_{\text{ELM}} = 17 \pm 1$ Hz for the gas-fueled reference case and $f_{\text{ELM}} = 59 \pm 14$ Hz for the pellet-fueled reference case. Across the fueling scan, f_{ELM} increases steadily to $f_{\text{ELM,max}} = 300 \pm 60$ Hz and is characterized by a wide variation in ELM sizes. This is characterized as a *mixed* regime, where large and small ELMs are both present [28]. Though the majority of the ELMs at higher density are small ELMs, the frequency of large ELMs, which are characterized by at least a 2% drop in plasma stored energy, still increases to ~ 80 Hz in the highest-fueled cases. The same effect is observed in line integrated density measurements, with the frequency of ELMs with at least a 2% drop in density saturating at ~ 80 Hz. Increasing ELM frequency with increasing fueling is consistent with ELM pacing and detachment studies, where increased fueling in the form of pellet pacing or gas puffs leads to decreased heat fluxes on PFCs through ELM mitigation. These physics processes can be utilized for control schemes as well, such as a processes developed on JET to use gas fueling as an actuator for ELM frequency control [44].

As the density increased with increased fueling, the energy lost during each ELM event decreased relative to the pedestal pressure. To quantify the variations in ELM size, the drop in plasma stored energy after each ELM (ΔW_{MHD}) was calculated with the EFIT code [43]. The average drop in plasma stored energy ΔW_{MHD} is shown in figure 8(b). All pellet-fueled cases ran at a stationary $W_{\text{MHD}} = 760$ kJ, whereas the gas-fueled cases dropped to $W_{\text{MHD}} = 520$ kJ compared to the reference (no gas) shot, which had $W_{\text{MHD}} = 570$ kJ. This is correlated with the pedestal pressure drop noted in figure 3. As the ELM frequency increased, the average ΔW_{MHD} per ELM decreased and the distribution of ΔW_{MHD} across all ELMs widened, as is shown in figure 9. In the gas-fueled discharges,

the higher-fueled shots demonstrated a broad range of ELMs sizes, all smaller than ELMs in the reference shot. ELMs in the pellet-fueled reference case (no pellets) were already more irregular than in the ‘no gas’ reference case, however, the same decreasing intensity trend was observed across the pellet-fueling scan, with $\Delta W_{\text{MHD}} / W_{\text{MHD}} \leq 4\%$ in the highest-fueled pellet discharge. As seen in figure 8, (which shows W_{MHD} as a function of time for the highest-fueled discharges,) many smaller ELM events are not correlated with a detectable drop in stored energy [45]. These events occurred throughout the two fueling scans and represent the small events reported in figure 9.

Because of the different ELM behaviors observed in the two reference cases, it is difficult to draw substantial conclusions on the effect of particle source location on the ELM characteristics from the discharges in this study. However, it should be noted that the pellet-fueled discharges never produced ELMs of the same magnitude as observed in similar shaped ECH and gas-fueled plasmas. This suggests that small, mitigated ELMs regimes exist readily within centrally-fueled discharges.

4.1. Peeling–ballooning instabilities

Changes in the pedestal structure (especially the pedestal width and the displacement between the temperature and density pedestal locations) are likely influential on the behavior of instabilities in the edge. According to the EPED1 model, these instabilities will then set limits on the achievable pedestal height and pressure gradient [46]. One of the most important instabilities in this regard is the peeling–ballooning mode (PBM), which is driven by coupling between steep pressure gradients and edge current densities. This

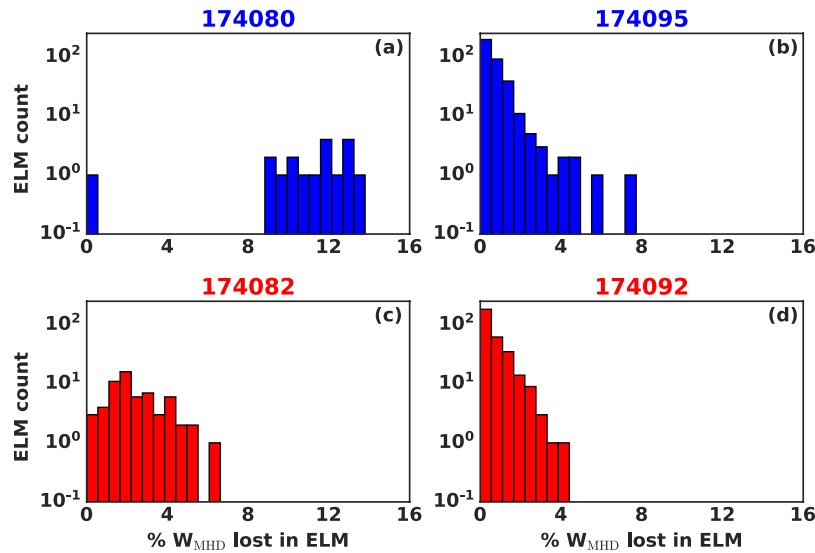


Figure 9. Histograms depicting size distribution of ELMs as measured by the fractional drop in W_{MHD} after an ELM for the (a) and (c) reference and (b) and (d) highest-fueled discharges. The ECH + gas puff shots are shown in blue; the NBI + pellet shots are shown in red.

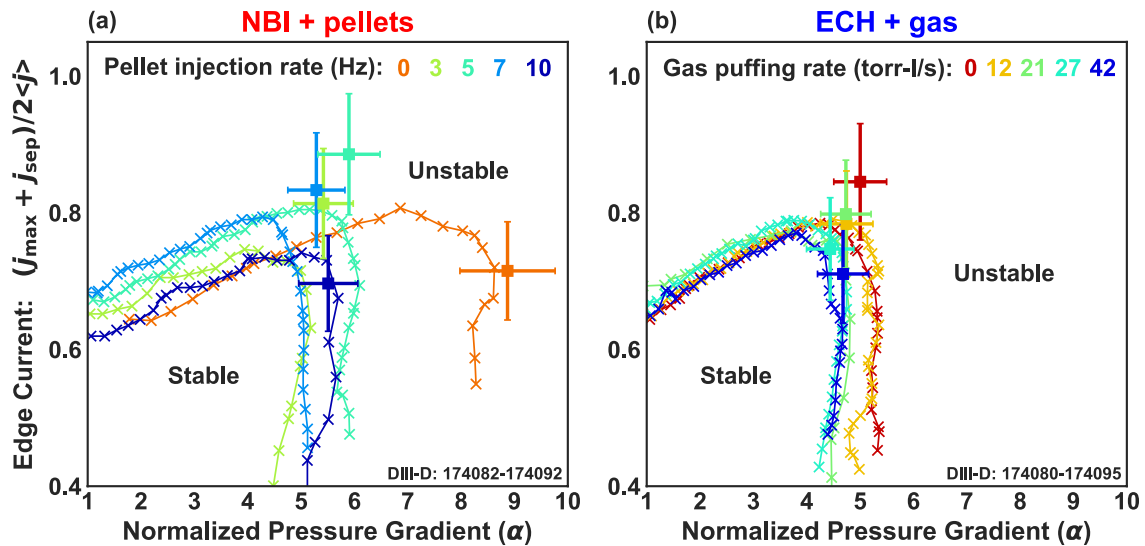


Figure 10. Stability boundaries calculated with ELITE for (a) the pellet-fueled discharges and (b) the gas-fueled discharges. Same-color profiles have similar total fueling rates.

instability is often associated with the triggering of ELMs when the pedestal reaches a critical height and crosses the PB stability threshold [47, 48]. The ELITE code was used to calculate the PB stability boundary for both sets of discharges. In this analysis, the pressure gradient and edge current that are used as constraints for each kinetic equilibrium are systematically varied around their experimental values. ELITE is then used to calculate the growth rate of each PBM leading up to the onset of an ELM crash. The edge current density is calculated as a function of minor radius and is the sum of bootstrap current, the NBI driven current and the Ohmic current from a neoclassical model, minus the (small) poloidal current. Iterations are performed to remap experimental data and readjust the current and pressure profiles based on each equilibria. The stability boundary is calculated

based on the diamagnetic stabilization effect derived from BOUT++ calculations [49].

Results of the ELITE stability analysis are presented in figure 10. Throughout the two fueling scans, the analyzed experimental cases are all near the nose of the PB stability boundary, suggesting that the obtained plasmas are driven unstable by large, type-I ELMs resulting from strongly coupled peeling and ballooning modes of moderate mode number. In the pellet-fueled discharges (figure 10(a)) a large reduction in the size of the stable region is observed after the injection of the first pellets. The large inward shift of the ballooning stability boundary is correlated with a strong reduction of the edge temperature gradient between 0 Hz and 3 Hz pellet injection, and suggests a robust change in the plasma stability. Additional pellet fueling has noticeable effects on the location

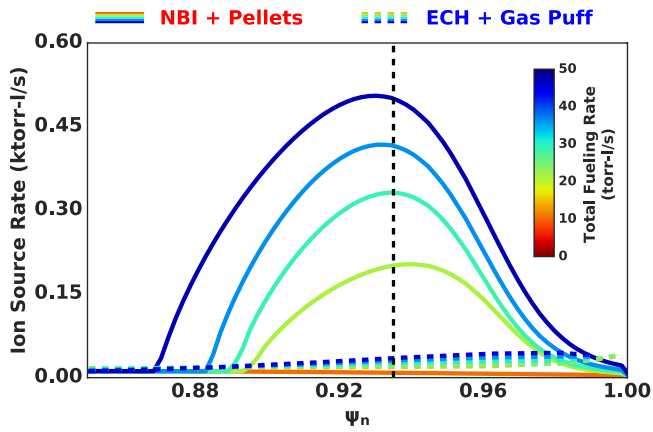


Figure 11. Ion source rate profiles (surface integral) for the discharges in this study. Pellet ablation profiles from PELLET are shown in solid lines, gas ionization profiles from UEDGE are shown in dashed lines. Same-color profiles have similar total fueling rates. The integral of each curve represents the total number of injected particles that penetrate the confined plasma region.

of the PB boundary, but never to the same degree. It should be emphasized that the smaller normalized pressure gradients in the pellet-fueled cases compared to the ‘no pellet’ baseline do not correspond to lower pedestal performance since the pedestal width increases to keep the total pedestal pressure constant. This relationship is reproduced by the EPED model, as discussed below. In figure 10(b), increases in the fueling rate for gas-fueled shots on a closed divertor are shown to shift the ballooning boundary slightly inwardly, as was previously noted on DIII-D [30]. To some extent, gas-fueled discharges with higher fueling are shifted away from moderate mode numbers at the nose of the PB boundary towards higher- n ballooning dominant locations in stability space.

5. Modeling of the particle source

The experimental phenomena described above lend strong support to the argument that the shape of the neutral fueling profile has a substantial effect on the structure of the H-mode pedestal. In order to further understand changes in the pedestal that result from fueling profile variations, a suite of modeling tools was used to characterize the transport and stability of each discharge.

5.1. Characterization of the fueling profile

The neutral fueling profiles for pellet-fueled and gas-fueled discharges are shown in figure 11. The pellet injection profiles are calculated with a stand-alone ablation model called PELLET [50]. The pellet is assumed to be immersed in quasi-steady dense neutral gas cloud that is responsible for shielding the pellet, allowing only a fraction of the incident energy to reach the surface and balance the energy lost through vaporization. As the pellet expands due to heating, it undergoes a transonic flow that is taken into account when the ablation rate and pellet lifetime are calculated [51]. PELLET computes the ablation rate of each fueling pellet as a function of the

distance along the pellet’s trajectory based on the geometry of the discharge and the experimentally measured density and temperature profiles. The total fueling rate in figure 11 is determined by multiplying the ablation profile of a single pellet by the pellet injection frequency to determine the total ablation rate per second. Ablation in the SOL is assumed to be negligible and is not included in the model. Within the experimentally obtained temperatures and densities, the computed pellet ablation profile peaks at the pedestal top (indicated by a dotted vertical line in figure 11) regardless of the plasma conditions. This confirms that pellets can be expected to deposit neutrals well inside the separatrix and throughout the pedestal and outer plasma region in DIII-D, in this case up to radii of $\psi_n \sim 0.88$. Note that due to drifts and transport, the large edge density perturbation can penetrate even further into the plasma, leading to an inverted density gradient as far in as $\psi_n \sim 0.6$ as seen in figure 4. To first order, higher pellet injection rates deposit more cold particles at the pedestal top. However, since additional fueling also lowers the plasma temperature, the high-frequency pellets are also able to penetrate further into the bulk plasma, directly cooling particles further inside the pedestal top. This can be seen in figure 4, where the PELLET ablation profile extends further towards the core plasma as the injection frequency increases. The presence of colder particles further inside the plasma decreases $\nabla T_{e,max}$ in the pedestal and increases the T_e pedestal width at the highest pellet fueling rates, as noted in the experimental observations above.

Also shown in figure 11 are the 1D ion source profiles in the confined plasma region for the gas-fueled cases, as calculated in the UEDGE code [52]. These profiles were obtained by automatically matching the experimentally measured outer midplane n_e , T_e and T_i profiles in UEDGE by changing the particle diffusion and the electron and ion heat conduction. Robust matching was done with a new algorithm based on local gradients with a 3% fixed fraction carbon, high recycling plates, standard flux limits turned on and a SOL simulation region that covered approximately 10 times the DIII-D heat flux decay length. The ion source rate was calculated as the neutral gas density multiplied by the ionization rate coefficient, per volume element. Individual neutrals from gas puffs have a more difficult time traversing the SOL than pellets and thus the majority of incoming neutrals are ionized near the wall before they cross the separatrix, leading to the lower absolute values of the ion source rate in the confined plasma region for the gas-fueled discharges seen in figure 11. While pellets are able to deliver neutral fuel well within the plasma at the pedestal top, gas puffs are primarily ionized near the wall and throughout the SOL. Gas puffs thus function more as *ion fueling* of the core plasma, as opposed to the *neutral fueling* achieved by pellet ablation. As observed above, this increases the SOL density and $n_{e,sep}$, but contributes less to the main plasma density. The difference between ion fueling and neutral fueling can also be observed quantitatively by calculating the fraction of injected particles that are ionized inside of the separatrix for the pellet and gas cases. In the pellet cases, almost 100% of the fuel is ionized within the separatrix

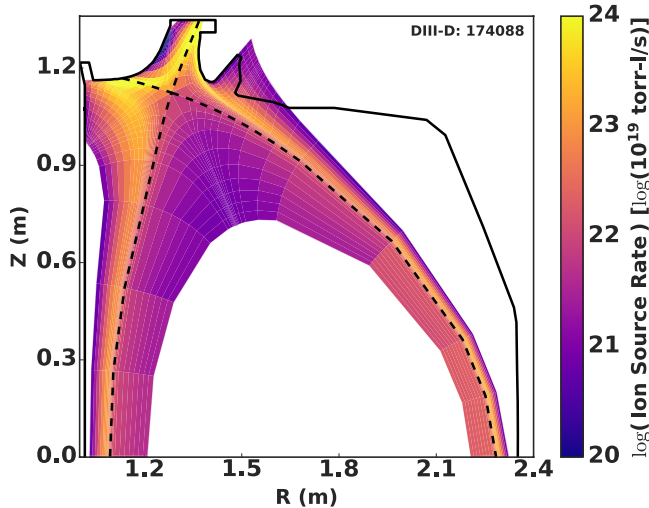


Figure 12. Calculated UEDGE ion source: deposition of the deuterium neutrals is mainly due to high ion recycling at the divertor plates rather than the direct ionization of the neutrals in front of the gas puffing system. The separatrix is shown as a dashed line.

since both NBI and pellet neutrals pass relatively unimpeded through the SOL. However, in the gas-fueled cases, the total number of fuel particles ionized inside of the separatrix drops from $\sim 30\%$ to just $\sim 15\%$ over the course of the fueling scan.

The 2D ion source profile for the lowest fueled (12.1 torr $l\ s^{-1}$) gas puff shot is shown in figure 12. While the neutral density is greater directly near the gas puff location, low T_e in the SOL allows neutral gas to move about the SOL before ionizing. Thus, the ion source rate appears radially located just outside of the confined plasma region at all poloidal locations. The calculated ion sources suggest a location for the deposition of the neutrals from gas puffing in UEDGE, i.e. mainly from the ion recycling at the plates rather than from the direct ionization of the neutrals near the gas puffing system. In general, the divertor particle flux from recycling can be much larger than that from direct gas fueling, though the efficiency is low [13]. From figure 11 we can see that pellets bypass this as a primary interaction, though deuterium exhaust from the main plasma may still be recycled in the divertors after $\sim 1\ \tau_p$. It is also important to note that, while the main ion source for the gas-fueled cases in figure 12 is in the upper divertor, significant ionization still exists just outside the separatrix at all poloidal angles. A full 2D investigation on the importance of particle drifts and pinches as a function of fueling location is beyond the scope of this paper and will be presented in later work.

5.2. Increased core transport with ECH heating

Though trends within each fueling scan are present, direct comparisons between the transport of shots with different heating schemes is difficult. This is highlighted in figure 13, where the electron thermal conductivity (χ_e) calculated in TRANSP [53, 54] is plotted for different discharges. All transport calculations were done in the stationary phase of the pellet cycle after the ablation density spike had relaxed,

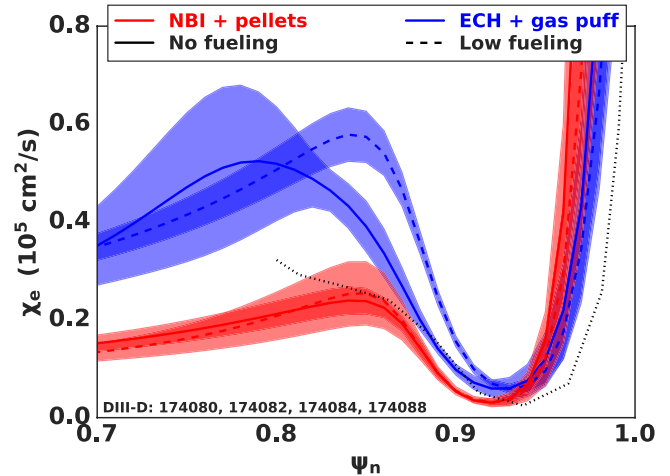


Figure 13. Electron heat conductivity (χ_e) calculated in TRANSP. Solid lines show χ_e for the reference cases with no fueling; dashed lines show χ_e for the lowest fueling cases (174084 and 174088). The ECH/gas-fueled shots show higher diffusivity throughout the pedestal region and the core plasma. The same transport coefficient calculated in UEDGE is shown as a black dotted line.

so the only particle source considered in TRANSP was from the edge and neutral beams. The conductivity profiles in the gas-fueled cases are well matched to the 1D χ_e profile at the outer midplane calculated automatically in UEDGE, which is shown as a dotted black line in figure 13. In figure 13, the transport coefficients for the two reference discharges (no-gas: 174080 and no-pellet: 174082) are shown as solid lines. Around the pedestal top location the two reference cases have similar transport coefficients. This is reflected in a $<10\%$ variation in χ_e between the two reference cases at the pedestal top. Further towards the core, however, χ_e is much larger in the ECH-heated discharge than the NBI-heated discharge, suggesting better core confinement from the NBI plasmas. Further, the NBI-heated discharges have a factor of ~ 2 higher energy confinement times than the ECH-heated discharges. When the fueling scan is conducted, the differences in χ_e become exaggerated. To illustrate this point, χ_e profiles for the lowest fueled cases are shown as dashed lines with one-standard-deviation error bars in figure 13. Gas fueling strongly shifts the steep gradient region of the ITB towards the edge, increasing the difference between $\chi_{e,pellet}$ and $\chi_{e,gas}$. The original difference in transport between the two fueling schemes is a result of both different particle source locations and different heating schemes, and the relative strength of each effect is difficult to disentangle. The effect of the heating scheme variation on the profile shape will be addressed in future work, where experiments will be run to isolate any effects resulting from the heating scheme discrepancy present above.

5.3. Comparison to the EPED1 model

Since the pedestal has a strong impact on the fusion performance, accurate prediction of the pedestal structure is an essential element of scenario design and optimization. Furthermore, a good model of the pedestal can help generate understanding of potential ELM behavior on ITER.

Established pedestal models have thus been designed to predict the pedestal structure based on the onset of non-local peeling–ballooning modes and nearly-local kinetic ballooning modes [47]. EPED1 is a model to predict the pedestal height and width at a given density and in a high-performance (type-I ELMs) discharge. It consists of two coupled hypothesis that limit the shape of the pedestal. First, low- to intermediate- n peeling–ballooning modes are expected to constrain the pedestal height. Second, the pedestal width is constrained based on the onset of high- n kinetic ballooning modes, which are short wavelength, pressure-driven instabilities. These constraints are calculated from a series of 2D model equilibrium subject to a maximum growth rate criteria, as is calculated in ELITE [47]. In this study, in addition to the eight traditional EPED1 inputs (B_t , I_p , R , a , δ , κ , $n_{e,\text{ped}}$ and β_N) the effective atomic charge in the pedestal (Z_{eff}) was also included. The EPED1 model has been shown to be in good agreement with data under typical ELMy plasma conditions both in small detailed studies and in large statistical surveys across multiple machines [47, 48, 55, 56]. It is important to note, however, that no full predictability of the pedestal is currently possible. For example, EPED1 requires input information on the pedestal top density and cannot predict the pedestal structure from sources alone. Further, EPED1 assumes alignment of the n_e and T_e pedestal profiles, which was not consistently observed experimentally. The role that neutral sources, among other things, play in setting the pedestal density has yet to be incorporated into these models.

Unsurprisingly, the EPED1 model, which does not directly take into account the particle source location, is unable to fully predict the changes observed in this fueling study. As seen in figure 14, where the pedestal height prediction from EPED1 is shown in open markers, the predicted pedestal height is in good agreement with the measured pedestal height for the gas-fueled discharges. In this case, the slight ($\sim 10\%$) over-prediction can be attributed to the mix of large and small ELMs observed in the experiment, which will slightly lower the pedestal height from the nominal EPED1 value, which expects large type-I ELMs. EPED1 is also able to qualitatively reproduce the higher total pedestal pressure observed in the pellet-fueled cases due to the higher Shafranov shift, β_N and $n_{e,\text{ped}}$ observed there. However, these parameter changes do not fully capture the quantitative difference in the height of the total pedestal pressure observed in experiment: the model consistently under predicts the pedestal height in the pellet-fueled discharges. In typical mixed-ELM discharges, EPED1 predictions can usually be taken as an upper-bound for the achievable pedestal performance. However, it appears from this data that a more centrally-located particle source location can increase the pedestal height above the EPED1 prediction. Under-prediction of the pedestal height with EPED1 has been noted before, for example at high deuterium fueling and with impurity seeding on JET [57, 58]. Efforts to predict the pedestal height for ITER based on the EPED1 model have proven valuable [49], but it should be noted that the more centrally-located fueling source and/or an opaque SOL will likely change the obtained pedestal structure. The difficult task of

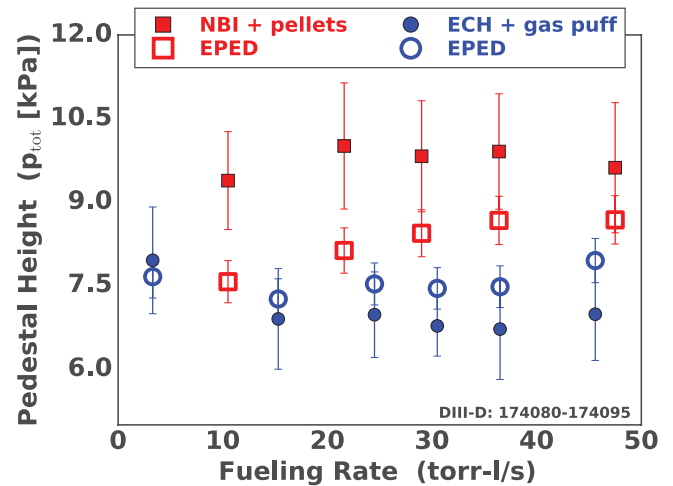


Figure 14. Height of the total pressure profile versus fueling rate. Experimental values are shown with solid marker; EPED1 predictions are shown with open markers. EPED1 is unable to reproduce the full change in the pedestal height observed between the two fueling schemes.

including the neutral fueling location into a predictive model for the pedestal height would be a profitable avenue for further work.

6. Summary and conclusions

In this dedicated experiment, the structure of the H-mode pedestal is shown to be highly dependent on the neutral source profile near the edge. Differences in core fueling with NBI has little effect on the pedestal structure, whereas differences in fueling near the pedestal with gas and pellets led to several structural changes. Many of the differences between pellets and gas are largely transient in nature, especially at the top of the pedestal. However, after $\sim 1 \tau_p$, the perturbed pellet-fueled profiles relax towards a stationary form that is similar to the gas-fueled pedestals. An increased pellet fueling frequency deposits more cold neutrals further inside the plasma, flattening and widening the stationary T_e pedestal. This contributes to a higher fueling efficiency for pellets. Further, the structure of the pedestal is shown to be altered after the injection of just a single pellet and the density does not recover to its original value long after the pellet ablation timescale. In contrast, increased gas fueling shifts the ionization profile further outwards, increasing the offset of the n_e and T_e pedestals and raising $n_{e,\text{sep}}$. Analysis of the ablation profiles with PELLET showed that higher frequency pellets were able to penetrate further into the confined region since the bulk plasma temperature was lowered. For a more edge localized particle source UEDGE analysis showed that, even at the highest fueling rates, ionization from gas puffing remained predominantly outside of the separatrix. High neutral fueling in the SOL from gas puffs was shown to preserve the ratio $n_{e,\text{ped}}/n_{e,\text{sep}}$. This ratio was not preserved with pellet fueling, suggesting that fueling scans can be effective tools to enable studies of pedestal behavior under a wide variety of pedestal gradients. The obtained variations

in pedestal structure were shown to influence plasma stability and core impurity content across several discharges with constant $p_{e,ped}$. Notably, observations presented in this work stress the importance of determining the compatibility of proposed ITER scenarios with pellet fueling. The EPED1 code consistently under-predicted the total pedestal height in the pellet-fueled discharges. Extrapolations based on gas-fueled pedestal structure may miss key changes in the pedestal structure that could have significant implications. Assessing the impact of core-localized fueling profiles in high-performance scenarios should be addressed in the ongoing work supporting next-generation scenario development.







Acknowledgments

The authors would like to thank J. Sachdev, T.H. Osborne, P.B. Snyder and M. Knolker for their assistance in this work. Part of data analysis was performed using the OMFIT integrated modeling framework [40]. This material is based upon work supported by the U.S. Department of Energy, Office of Science, Office of Fusion Energy Sciences, using the DIII-D National Fusion Facility, a DOE Office of Science user facility, under Awards DC-AC02-09CH11466, DE-SC0015480, DE-SC0015878, DE-FC02-04ER54698, and DE-AC05-00OR22725.

Disclaimer

This report was prepared as an account of work sponsored by an agency of the United States Government. Neither the United States Government nor any agency thereof, nor any of their employees, makes any warranty, express or implied, or assumes any legal liability or responsibility for the accuracy, completeness, or usefulness of any information, apparatus, product, or process disclosed, or represents that its use would not infringe privately owned rights. Reference herein to any specific commercial product, process, or service by trade name, trademark, manufacturer, or otherwise, does not necessarily constitute or imply its endorsement, recommendation, or favoring by the United States Government or any agency thereof. The views and opinions of authors expressed herein do not necessarily state or reflect those of the United States Government or any agency thereof.

ORCID iDs

A.O. Nelson  <https://orcid.org/0000-0002-9612-1936>
 F.M. Laggner  <https://orcid.org/0000-0003-1601-2973>
 B.A. Grierson  <https://orcid.org/0000-0001-5918-6506>
 O. Izacard  <https://orcid.org/0000-0002-5949-8427>
 D. Eldon  <https://orcid.org/0000-0003-1895-0648>
 M.W. Shafer  <https://orcid.org/0000-0001-9808-6305>
 A. Leonard  <https://orcid.org/0000-0001-9356-1074>
 A.C. Sontag  <https://orcid.org/0000-0003-1223-5985>
 E. Kolemen  <https://orcid.org/0000-0003-4212-3247>

References

- [1] Osborne T.H. et al 1998 *Plasma Phys. Control. Fusion* **40** 845
- [2] ITER Physics Expert Group on Confinement and Transport 1999 *Nucl. Fusion* **39** 2175
- [3] Doyle E.J. et al 2007 *Nucl. Fusion* **47** S18–127
- [4] Mahdavi M.A. et al 2003 *Phys. Plasmas* **10** 3984
- [5] Fenstermacher M.E. et al 2005 *Nucl. Fusion* **45** 1493–502
- [6] Dunne M.G. et al 2017 *Plasma Phys. Control. Fusion* **59** 014017
- [7] Garzotti L. et al 2012 *Nucl. Fusion* **52** 013002
- [8] Lehnert B. 1968 *Nucl. Fusion* **8** 173
- [9] Kukushkin A.S. et al 2003 *Nucl. Fusion* **43** 716
- [10] Hughes J.W. et al 2006 *Phys. Plasmas* **13** 056103
- [11] Hughes J.W. et al 2007 *Nucl. Fusion* **47** 1057
- [12] Beurskens M.N.A. et al 2013 *Plasma Phys. Control. Fusion* **55** 124043
- [13] Petrie T.W. et al 1997 *Nucl. Fusion* **37** 321
- [14] Leonard A.W. et al 2015 *J. Nucl. Mater.* **463** 519–23
- [15] Petrie T.W. et al 2017 *Nucl. Fusion* **57** 086004
- [16] Baylor L.R. et al 2007 *Nucl. Fusion* **47** 443
- [17] Baylor L.R. et al 2009 *Nucl. Fusion* **49** 085013
- [18] Polevoi A.R. et al 2017 *Nucl. Fusion* **57** 022014
- [19] Lang P.T. et al 2004 *Nucl. Fusion* **44** 665
- [20] Lang P.T. et al 2011 *Nucl. Fusion* **51** 033010
- [21] Baylor L.R. et al 2013 *Phys. Rev. Lett.* **110** 245001
- [22] Lang P.T. et al 2014 *Nucl. Fusion* **54** 083009
- [23] Polevoi A.R. et al 2018 *Nucl. Fusion* **58** 056020
- [24] Lang P.T. et al 2018 *Nucl. Fusion* **58** 036001
- [25] Greenwald M. et al 1984 *Phys. Rev. Lett.* **53** 352–5
- [26] Kamada Y. et al 2002 *Plasma Phys. Control. Fusion* **44** A279
- [27] Baylor L.R. et al 2003 *J. Nucl. Mater.* **313–6** 530–3
- [28] Harrer G.F. et al 2018 *Nucl. Fusion* **58** 112001
- [29] Garzotti L. et al 2014 *Plasma Phys. Control. Fusion* **56** 035004
- [30] Wang H.Q. et al 2018 *Nucl. Fusion* **58** 096014
- [31] Baylor L.R. et al 2001 *J. Nucl. Mater.* **290–3** 398–401
- [32] Valović M. et al 2008 *Nucl. Fusion* **48** 075006
- [33] Carlstrom T.N. et al 1992 *Rev. Sci. Instrum.* **63** 4901
- [34] Eldon D. et al 2012 *Rev. Sci. Instrum.* **83** 10E343
- [35] Chrystal C. et al 2016 *Rev. Sci. Instrum.* **87** 11E512
- [36] Eldon D. et al 2020 Private communication
- [37] Sauter O. et al 1999 *Phys. Plasmas* **6** 2834–9
- [38] Groebner R.J. et al 2001 *Nucl. Fusion* **41** 1789
- [39] Stangeby P.C. et al 2015 *Nucl. Fusion* **55** 093014
- [40] Meneghini O. et al 2015 *Nucl. Fusion* **55** 083008
- [41] Logan N.C. et al 2018 *Fusion Sci. Technol.* **74** 125–34
- [42] Baylor L.R. et al 2005 *J. Nucl. Mater.* **337–9** 535–8
- [43] Lao L.L. et al 1985 *Nucl. Fusion* **25** 1611
- [44] Lennholm M. et al 2015 *Nucl. Fusion* **55** 063004
- [45] Bortolon A. et al 2016 *Nucl. Fusion* **56** 056008
- [46] Snyder P.B. et al 2002 *Phys. Plasmas* **9** 2037–43
- [47] Snyder P.B. et al 2009 *Phys. Plasmas* **16** 056118
- [48] Snyder P.B. et al 2012 *Phys. Plasmas* **19** 056115
- [49] Snyder P.B. et al 2011 *Nucl. Fusion* **51** 103016
- [50] Houlber W. et al 1988 *Nucl. Fusion* **28** 595
- [51] Parks P.B. et al 1978 *Phys. Fluids* **21** 1735
- [52] Rognien T.D. et al 1992 *J. Nucl. Mater.* **196–8** 347–51
- [53] Breslau J. et al 2018 *Transport* (<https://doi.org/10.11578/dc.20180627.4>)
- [54] Grierson B.A. et al 2018 *Fusion Sci. Technol.* **74** 101–15
- [55] Groebner R.J. et al 2013 *Nucl. Fusion* **53** 093024
- [56] Beurskens M.N.A. et al 2011 *Phys. Plasmas* **18** 056120
- [57] Leyland M.J. et al 2013 *Nucl. Fusion* **53** 083028
- [58] Leyland M.J. et al 2015 *Nucl. Fusion* **55** 013019